Design and Analysis of a Symmetric Joint Module for a Modular Wire-Actuated Robotic Arm with Symmetric Variable-Stiffness Units

Can Qian , Kaisheng Yang * , Yangfei Ruan , Junhao Hu , Zixuan Shao , Chongchong Wang , Chuanqi Xie

Posted Date: 16 May 2024

doi: 10.20944/preprints202405.1069.v1

Keywords: wire-actuated robot; service robot; human-robot interaction; variable-stiffness unit

Article

Design and Analysis of a Symmetric Joint Module for a Modular Wire-Actuated Robotic Arm with Symmetric Variable-Stiffness Units

Can Qian [1], Kaisheng Yang [1,2,*], Yangfei Ruan [1], Junhao Hu [1], Zixuan Shao [1], Chongchong Wang [3] and Chuanqi Xie [4]

[1] Zhejiang Key Laboratory of Part Rolling Technology, Ningbo University, Ningbo 315211, China; 2311090171@nbu.edu.cn (C.Q.); yangkaisheng@nbu.edu.cn (K.Y.); 2311090176@nbu.edu.cn (Y.R.); 2311090118@nbu.edu.cn (J.H.); 2957068660@qq.com (Z.S.)

[2] Department of Automation, Shanghai Jiao Tong University, Shanghai 200240, China;

[3] AUBO (Beijing) Robotic Technology Company, Beijing 100195, China; wangchongchong@aubo-robotics.cn (C.W.)

[4] State Key Laboratory for Managing Biotic and Chemical Threats to the Quality and Safety of Agro-Products, Institute of Animal Husbandry and Veterinary Science, Zhejiang Academy of Agricultural Sciences, Hangzhou 310021, China; cqxie@zaas.ac.cn (C.X.)

* Correspondence: yangkaisheng@nbu.edu.cn

Abstract: In this paper, a modular wire-actuated robotic arm was designed to improve the safety and adaptability of service robots during human-robot interaction. To raise the stiffness adjustment range of the robotic arm, a symmetric variable-stiffness unit was designed based on flexure, which had compact and simple structure, and lowly nonlinear stiffness-force relationship. In this paper, we focused on the research of the symmetric 1-DOF joint module. Based on the kinematics and stiffness analysis, the pose of the joint module could be adjusted by controlling the length of the wires, and the stiffness of the joint module could be adjusted by controlling the tension of the wires. Because of the actuation redundancy, the pose and stiffness of the joint module could be controlled synchronously. Furthermore, a directly method was proposed for the stiffness-oriented wire tension distribution problem of the 1-DOF joint module. A simulation was carried out to verify the proposed method.

Keywords: wire-actuated robot; service robot; human-robot interaction; variable-stiffness unit

1. Introduction

Service robots usually work in the unstructured environment and interact with human. This requires the service robots to be safe and adaptive. While the traditional rigid robots always have heavy weight and high stiffness, which are not safe enough for human-robot interaction. In the past decades, soft robots have attracted researchers' attention, due to their great potential to interact with the human and the environment more safely and more adaptively[1,2].

The human arm mainly composes of bones, joints and muscles. Since the human arm is actuated by the soft muscles and the stiffness of the human arm can be adjusted by controlling the muscle strength, it can work in our daily life safely and adaptively. Inspired by the human arm, wire-actuated robotic arms are proposed to improve the safety and adaptability of service robots during human-robot interaction.

The wire-actuated robot is a kind of soft parallel robots, which employs the soft wires instead of rigid links to actuate the robot. Comparing with the rigid robots, wire-actuated robots have the advantages of low inertia, large workspace, high safety and adaptability. Because of these advantages, the wire-actuated robots are applied widely in many fields, such as lifting and positioning [3,4], detection and maintenance [5–7], wearable rehabilitation and assistance [8–13], medical surgery [14–16], soft robot arm and hand [17–20], bionic robot [21]. Researchers have

 doi:10.20944/preprints202405.1069.v1

designed different wire-actuated robots and carry out a lot of research works, such as kinematics and statics analysis [22–26], workspace analysis [27,28], wire tension analysis [29], stiffness analysis [30], dynamics analysis [31,32], path and trajectory planning [33–35], motion and compliance control [36–40] and so on. These works are valuable for the subsequent researches and applications of the wire-actuated robots.

In this paper, we adopted modular design method to design a wire-actuated human-like robotic arm, which could simplify the structure of the robotic arm and make it easy to analyze, control, reconstruct and maintain. The modular wire-actuated robotic arm consisted of three joint modules in series, i.e., a 3-DOF shoulder joint module, a 1-DOF elbow joint module, and a 3-DOF wrist joint. The wire actuation units were located at the base of the robotic arm. Since the wires had the property of unidirectional force transmission, the wire-actuated robotic arm was redundantly actuated, and the stiffness of the robotic arm could be adjusted by controlling the wire tensions. These features made the proposed modular wire-actuated robotic arm have low inertia, high load-to-weight ratio, large workspace, variable stiffness and high safety. Due to the limitation of the wire stiffness, the stiffness variation of the wire-actuated robotic arm was small. To raise the stiffness adjustment range, a variable-stiffness unit (VSU) was designed to place in the wire actuation system [41]. However, the existing VSUs generally had some following shortcomings [42–44]: (1) the VSU was made up with several parts, which was complex, large and heavy. (2) The assembly of the VSUs could not keep them same. (3) the stiffness-force relationship of the VSU was highly nonlinear. In this paper, a novel VSU was proposed based on the flexure, which had simple, symmetric and compact structure, and lowly nonlinear stiffness-force relationship. Furthermore, because of the redundant actuation property, the wires of the joint modules and the robotic arm could be divided into two groups: one for pose control and another for stiffness control. The pose could be adjusted by controlling the length of the wires, and the stiffness could be adjusted by controlling the tension of the wires. It meant that the pose and stiffness of the joint modules and robotic arm could be controlled synchronously. In order to achieve the desired stiffness of the joint module or robotic arm, the stiffness-oriented wire tension distribution (SWTD) problem should be solved. For multiple-DOF joint module, since the stiffness model was complicated, it was always difficult to solve the SWTD problem directly. The SWTD problem would be transferred into an optimization problem [45]. In this paper, we focused on the kinematics, statics, stiffness and wire tension analysis of the 1-DOF joint module, and the stiffness analysis of the VSU. The SWTD problem of the 1-DOF joint module was solved directly based on the statics and stiffness analysis. A simulation was carried out to verify the proposed analysis.

2. Design of a Modular Wire-Actuated Robotic Arm with Symmetric Variable-Stiffness Devices

Inspired by the human arm, a wire-actuated robotic arm was designed in this paper, in which the rigid links were employed to instead of the skeleton of the human arm and the flexible steel wires were employed to instead of the muscles of the human arm. For the convenience of fabrication and maintenance, the wire-actuated robotic arm was made up of three joint modules: shoulder joint module, elbow joint module and wrist joint module. The three joint modules were connected in series to build a modular wire-actuated robot arm, as shown in Figure 1. The end of each wire for the robotic arm was connected with the wire actuation unit. All the wire actuation units were installed on the base of the robotic arm. This arrangement could reduce the moment of inertia and improve the security of the robot.

Preprints.org (www.preprints.org) | NOT PEER-REVIEWED | Posted: 16 May 2024 doi:10.20944/preprints202405.1069.v1

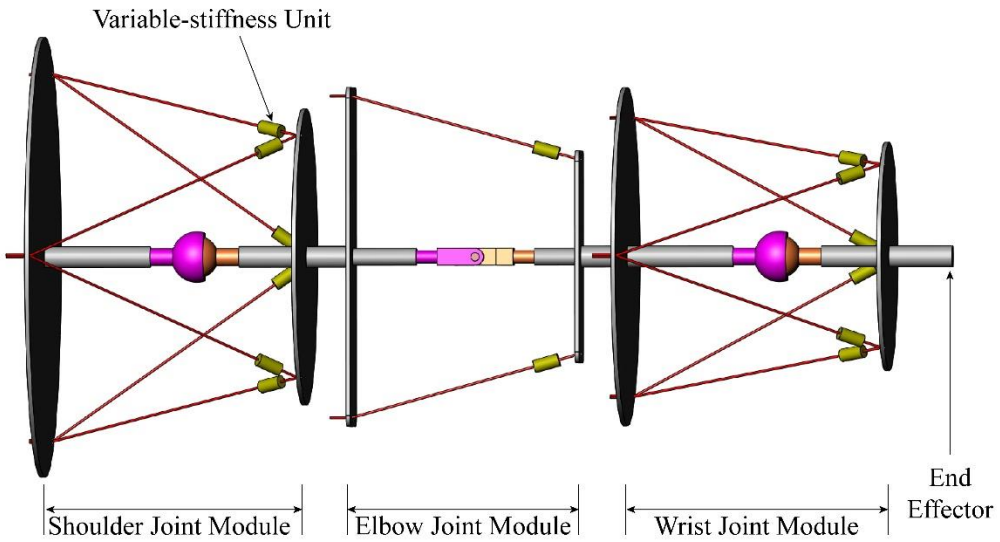

Figure 1. Conceptual design of the modular wire-actuated robotic arm.

The three joint modules of the modular wire-actuated robotic arm could be divided into two types: one-degree-of-freedom (1-DOF) joint module and three-degree-of-freedom (3-DOF) joint module. The conceptual design of the 1-DOF and 3-DOF joint module were shown in Figure 2. The 1-DOF joint module had symmetric structure and consisted of a movable platform, a static platform, a revolute joint, and wires. The 3-DOF joint module consisted of a movable platform, a static platform, a spherical joint, and wires. Since the variation range of the steel wire was limited, a variable-stiffness unit (VSU) was developed and placed along the wire to raise the variable-stiffness range of the robotic arm and improve its flexibility and safety.

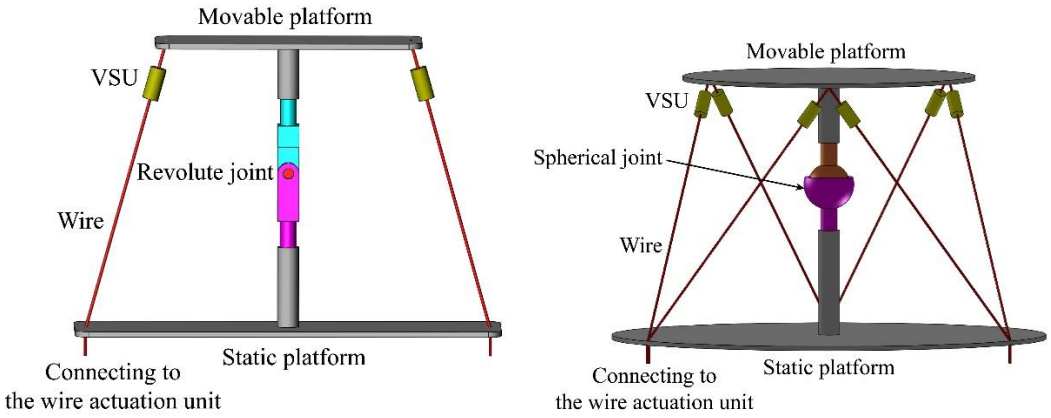

(**a**) (**b**)

Figure 2. Conceptual design of joint modules: (a) 1-DOF joint module; (b) 3-DOF joint module.

However, the existing VSUs generally had complex structure, large volume, heavy mass, and highly nonlinear stiffness-force relationship. In order to overcome these disadvantages, a novel VSU was proposed based on the flexure in this paper. As shown in Figure 3, the proposed VSU had simple, symmetric and compact structure. The VSU had a rhombus frame, denoted by ABCD. When the force $t_v \in \mathbb{R}$ acted at the point A and C, the VSU would deform. Due to the symmetric structure, we only need to analyze the deformation behavior of one side of the VSU. In this paper, the finite element method was employed to analyze the deformation of the VSU. The deformations of one side of the VSU were investigated under different forces. The results of the finite element analysis were shown in Figure 4.

 doi:10.20944/preprints202405.1069.v1

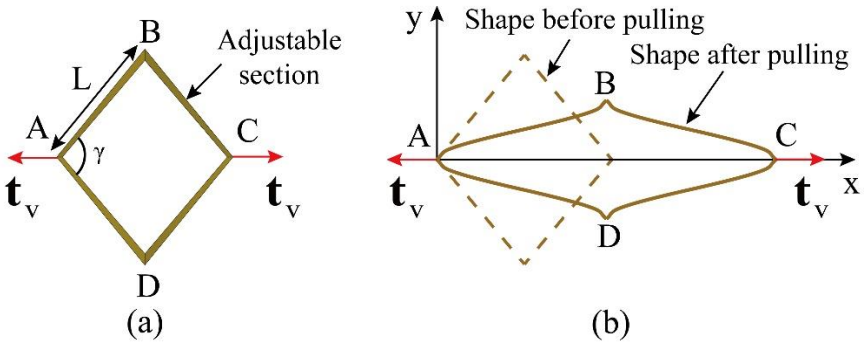

Figure 3. Design of the variable-stiffness unit (VSU): **(a)** diagram of the VSU; **(b)** deformation of the VSU after pulling.

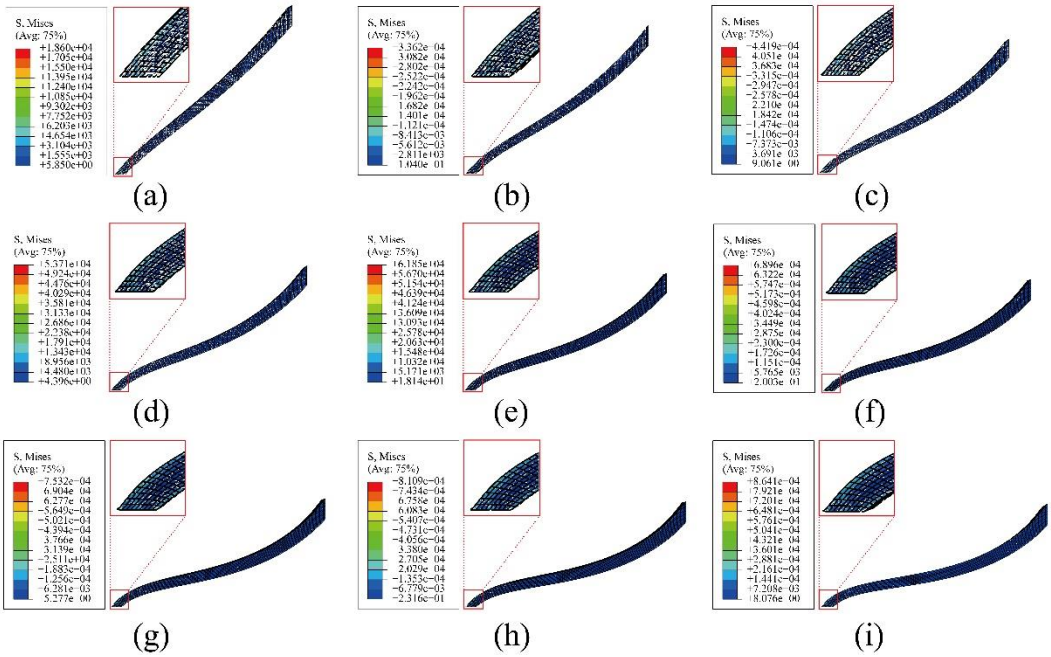

Figure 4. FEA for one side of the VSU under different loads: (a) $t_v = 100$ N; (b) $t_v = 200$ N; (c) $t_v = 300$ N; (d) $t_v = 400$ N; (e) $t_v = 500$ N; (f) $t_v = 600$ N; (g) $t_v = 700$ N; (h) $t_v = 800$ N; (i) $t_v = 900$ N.

Based on the FEA results, the stiffness-force relationship of the VSU yielded the following fitted function

$$k_v = 0.47t_v^2 + 118.05t_v + 21852.34 \quad (1)$$

where $k_v \in \mathbb{R}$ was the VSU stiffness, $t_v \in \mathbb{R}$ was the force acted on the VSU. The curve of the fitted function was shown in Figure 5, which had lowly nonlinear.

 doi:10.20944/preprints202405.1069.v1

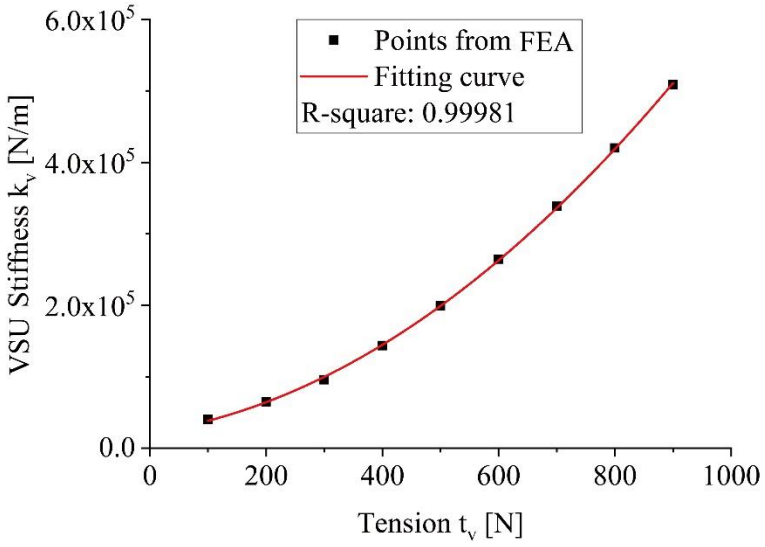

Figure 5. Stiffness-force relationship of the VSU.

3. Kinematics Modelling and Analysis of the Symmetric Joint Module

In the 1-DOF joint module, the movable platform rotated around the center O of the revolute joint with respect to the static platform. Two coordinate systems were established at the center O of the revolute joint: the coordinate system {M} which was attached to the movable platform and the coordinate system {S} which was attached to the static platform. When the two coordinate systems coincided with each other, the joint module was said to be in the home pose, also known as the initial pose.

Based on the two coordinate systems, the pose of the movable platform relative to the static platform could be described by the pose of the coordinate system {M} relative to the coordinate system {S}, which could be expressed mathematically by the rotation matrix $\mathbf{R} \in SO(3)$. Here $SO(3)$ represented Special Orthogonal group. Since the 1-DOF joint module had only one rotational degree of freedom, and the rotation only occurred in the OYZ plane of the coordinate system {S}, the pose of the movable platform relative to the static platform could be described by the rotational angle $\theta_{\mathrm{x}} \in \left(-\frac{\pi}{2}, \frac{\pi}{2}\right)$ about the X axis of {S}. That meant the rotation matrix $\mathbf{R} \in SO(3)$ could be determined by only one parameter θ_{x}, which satisfied:

$$\mathbf{R} = \begin{pmatrix} 1 & 0 & 0 \\ 0 & \cos\theta_{\mathrm{x}} & -\sin\theta_{\mathrm{x}} \\ 0 & \sin\theta_{\mathrm{x}} & \cos\theta_{\mathrm{x}} \end{pmatrix} \tag{2}$$

When the 1-DOF joint module was in the home pose, $\theta_{\mathrm{x}} = 0$. When the movable platform rotated in the positive direction of the X axis, $\theta_{\mathrm{x}} > 0$. When the movable platform rotated in the negative direction of the X axis, $\theta_{\mathrm{x}} < 0$.

Writing $m_i = \overline{\mathrm{OM}_i} \in \mathbb{R}$ $(i = 1, 2)$ as the distance of two points O and M_i, and $s_i = \overline{\mathrm{OS}_i} \in \mathbb{R}$ $(i = 1, 2)$ as the distance of two points O and S_i, then for a given 1-DOF joint module, the parameters m_i and s_i were constant. Writing $\varphi_i = \angle \mathrm{M}_i\mathrm{OS}_i \in \mathbb{R}$ $(i = 1, 2)$ as the angle between the two lines OM_i and OS_i, when the 1-DOF joint module was in the home pose, the initial value of φ_i was written as $\varphi_{i,0}$, which satisfied

$$\varphi_{i,0} = \pi - \angle \mathrm{M}_i\mathrm{OO}_{\mathrm{M}} - \angle \mathrm{S}_i\mathrm{OO}_{\mathrm{S}} \tag{3}$$

 doi:10.20944/preprints202405.1069.v1

For a given 1-DOF joint module, $\varphi_{i,0}$ was constant. When the movable platform rotated by the angle θ_x from the home pose, φ_i yielded:

$$\varphi_1 = \varphi_{1,0} + \theta_{\mathrm{x}} \tag{4}$$

$$\varphi_2 = \varphi_{2,0} - \theta_{\mathrm{x}} \tag{5}$$

Writing $c_i = \overline{\mathrm{M}_i\mathrm{S}_i} \in \mathbb{R}$ $(i=1,2)$ as the wire length between two points M_i and S_i, then the parameters c_i and φ_i yielded:

$$c_i^2 = m_i^2 + s_i^2 - 2m_i s_i \cos\varphi_i \tag{6}$$

Substituting (4) and (5) into (6), then the wire length c_i $(i=1,2)$ satisfied the following equations when the movable platform rotated by the angle θ_x from the home pose, i.e.,

$$c_1^2 = m_1^2 + s_1^2 - 2m_1 s_1 \cos\varphi_1 = m_1^2 + s_1^2 - 2m_1 s_1 \cos(\varphi_{1,0} + \theta_{\mathrm{x}}) \tag{7}$$

$$c_2^2 = m_2^2 + s_2^2 - 2m_2 s_2 \cos\varphi_2 = m_2^2 + s_2^2 - 2m_2 s_2 \cos(\varphi_{2,0} - \theta_{\mathrm{x}}) \tag{8}$$

From (7) and (8), it could be concluded that the wire length c_i $(i=1,2)$ was determined by the angle θ_x. On the other hand, the desired pose θ_x of the 1-DOF joint module could be reached by controlling the wire length c_i $(i=1,2)$.

Differentiating on both sides of (7) and (8), we had the following results:

$$\dot{c}_1 = \frac{m_1 s_1}{c_1}\sin(\varphi_{1,0} + \theta_{\mathrm{x}})\dot{\theta}_{\mathrm{x}} \tag{9}$$

$$\dot{c}_2 = -\frac{m_2 s_2}{c_2}\sin(\varphi_{2,0} - \theta_{\mathrm{x}})\dot{\theta}_{\mathrm{x}} \tag{10}$$

Writing $\mathbf{l}_{\mathrm{c}} = \begin{pmatrix} c_1 & c_2 \end{pmatrix}^{\mathrm{T}} \in \mathbb{R}^2$, where c_i $(i=1,2)$ was the wire lengths of the 1-DOF joint module, then (9) and (10) could be written in the following matrix form:

$$\dot{\mathbf{l}}_{\mathrm{c}} = \mathbf{J}_{\mathrm{x}}\dot{\theta}_{\mathrm{x}} \tag{11}$$

Here $\mathbf{J}_{\mathrm{x}} \in \mathbb{R}^{2\times 1}$ was the Jacobian matrix, which yielded:

$$\mathbf{J}_{\mathrm{x}} = \begin{pmatrix} \frac{m_1 s_1}{c_1}\sin(\varphi_{1,0} + \theta_{\mathrm{x}}) \\ -\frac{m_2 s_2}{c_2}\sin(\varphi_{2,0} - \theta_{\mathrm{x}}) \end{pmatrix} \tag{12}$$

Writing $\omega_{\mathrm{x}} = \dot{\theta}_{\mathrm{x}} \in \mathbb{R}$ as the angular velocity of the coordinate system {M} relative to the coordinate system {S} about the X axis of {S}, then (11) could be written as:

$$\dot{\mathbf{l}}_{\mathrm{c}} = \mathbf{J}_{\mathrm{x}}\omega_{\mathrm{x}} \tag{13}$$

 doi:10.20944/preprints202405.1069.v1

From (13), for a given pose of the 1-DOF joint module, the change rate of the wire lengths, $\dot{\mathbf{l}}_c$, was determined by the angular velocity, ω_x. On the other hand, the rotational velocity ω_x could be adjusted by controlling the change rate of the wire lengths.

Based on the parameters θ_x and ω_x in the OYZ plane of coordinate system {S}, the angle vector $\boldsymbol{\theta} \in \mathbb{R}^3$ and angular velocity $\boldsymbol{\omega} \in \mathbb{R}^3$ of the 1-DOF joint module in coordinate system {S} could be written as following

$$\boldsymbol{\theta} = \begin{pmatrix} \theta_x \\ 0 \\ 0 \end{pmatrix} \tag{14}$$

$$\boldsymbol{\omega} = \begin{pmatrix} \omega_x \\ 0 \\ 0 \end{pmatrix} = \begin{pmatrix} \dot{\theta}_x \\ 0 \\ 0 \end{pmatrix} = \dot{\boldsymbol{\theta}} \tag{15}$$

According to the exponential formula, the rotation matrix $\mathbf{R} \in SO(3)$ of {M} relative to {S} could be written as following

$$\mathbf{R} = e^{\hat{\boldsymbol{\omega}} t} = e^{\hat{\boldsymbol{\theta}}} \tag{16}$$

where the operator $\hat{(\bullet)}$ was defined by

$$\boldsymbol{\omega} = \begin{pmatrix} \omega_x \\ \omega_y \\ \omega_z \end{pmatrix} \rightarrow \hat{\boldsymbol{\omega}} = \begin{pmatrix} 0 & -\omega_z & \omega_y \\ \omega_z & 0 & -\omega_x \\ -\omega_y & \omega_x & 0 \end{pmatrix} \tag{17}$$

Then, in the coordinate system {S}, (13) could be expressed as following

$$\dot{\mathbf{l}}_c = \mathbf{J}\boldsymbol{\omega} \tag{18}$$

where the Jacobian matrix $\mathbf{J} \in \mathbb{R}^{2\times 3}$ yielded:

$$\mathbf{J} = \begin{pmatrix} \mathbf{J}_x & \mathbf{0} & \mathbf{0} \end{pmatrix} = \begin{pmatrix} \dfrac{m_1 s_1}{c_1} \sin(\varphi_{1,0} + \theta_x) & 0 & 0 \\ -\dfrac{m_2 s_2}{c_2} \sin(\varphi_{2,0} - \theta_x) & 0 & 0 \end{pmatrix} \tag{19}$$

For a given pose of the 1-DOF joint module, the Jacobian matrix $\mathbf{J} \in \mathbb{R}^{2\times 3}$ was constant. From (18), for a given pose of the 1-DOF joint module, the change rate of the wire lengths, $\dot{\mathbf{l}}_c$, was determined by the angular velocity, $\boldsymbol{\omega}$. On the other hand, the rotational velocity $\boldsymbol{\omega}$ could be adjusted by controlling the change rate of the wire lengths.

4. Stiffness Modelling and Analysis of the Symmetric Joint Module

As shown in Figure 6, the external force and torque acted on the movable platform of the 1-DOF joint module were denoted as $\mathbf{f}_{ex} \in \mathbb{R}^3$ and $\boldsymbol{\tau}_{ex} \in \mathbb{R}^3$, the tension of the i^{th} $(i = 1, 2)$ wire was denoted as $\mathbf{t}_i \in \mathbb{R}^3$, the force and torque acted on the revolute joint of the movable platform were

Preprints.org (www.preprints.org) | NOT PEER-REVIEWED | Posted: 16 May 2024 doi:10.20944/preprints202405.1069.v1

denoted as $\mathbf{f}_{\text{in}} \in \mathbb{R}^3$ and $\boldsymbol{\tau}_{\text{in}} \in \mathbb{R}^3$, respectively. In the coordinate system {S}, the movable platform of the 1-DOF joint module satisfied the following equilibrium equations

$$\mathbf{f}_{\text{ex}} + \mathbf{f}_{\text{in}} + \sum_{i=1}^{2} \mathbf{t}_i = \mathbf{0} \tag{20}$$

$$\boldsymbol{\tau}_{\text{ex}} + \boldsymbol{\tau}_{\text{in}} + \sum_{i=1}^{2} \mathbf{m}_i \times \mathbf{t}_i = \mathbf{0} \tag{21}$$

where $\mathbf{m}_i = \overrightarrow{\text{OM}_i} \in \mathbb{R}^3 \ (i = 1,2)$.

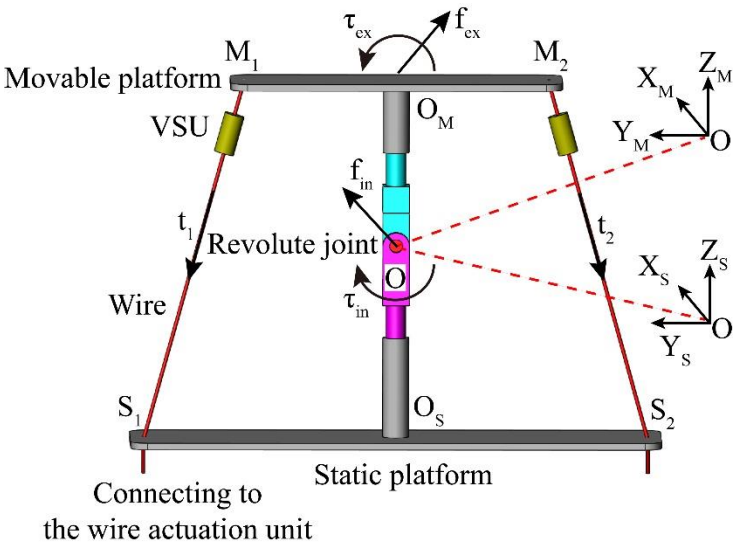

Figure 6. Diagram of the 1-DOF joint module.

Writing $\mathbf{c}_i = \overrightarrow{\text{M}_i\text{S}_i} \in \mathbb{R}^3 \ (i = 1,2)$ and defining $\mathbf{u}_i = \dfrac{\mathbf{c}_i}{c_i} \in \mathbb{R}^3$ as the unit vector along the $i^{\text{th}} \ (i = 1,2)$ wire of the 1-DOF joint module, then the tension $\mathbf{t}_i$ of the $i^{\text{th}} \ (i = 1,2)$ wire could be written as

$$\mathbf{t}_i = t_i \mathbf{u}_i \tag{22}$$

where $t_i = |\mathbf{t}_i| \in \mathbb{R}$ represented the value of the wire tension $\mathbf{t}_i$. Thus the equilibrium equations (20) and (21) could be written as:

$$\mathbf{f}_{\text{ex}} + \mathbf{f}_{\text{in}} = -\sum_{i=1}^{2} \mathbf{u}_i t_i = -\mathbf{U}\ \mathbf{T} \tag{23}$$

$$\boldsymbol{\tau}_{\text{ex}} + \boldsymbol{\tau}_{\text{in}} = -\sum_{i=1}^{2} \mathbf{m}_i \times \mathbf{t}_i = -\sum_{i=1}^{2} (\mathbf{m}_i \times \mathbf{u}_i) t_i = \mathbf{J}^{\text{T}}\ \mathbf{T} \tag{24}$$

where $\mathbf{T} = \begin{pmatrix} t_1 & t_2 \end{pmatrix}^{\text{T}} \in \mathbb{R}^2$ was a vector composed of the values of the wire tension $t_i \ (i = 1,2)$, and $\mathbf{U} = \begin{pmatrix} \mathbf{u}_1 & \mathbf{u}_2 \end{pmatrix} \in \mathbb{R}^{3\times 2}$ was a matrix composed of the unit vector $\mathbf{u}_i \ (i = 1,2)$, $\mathbf{J} \in \mathbb{R}^{2\times 3}$ represented the Jacobian matrix and its transposed matrix $\mathbf{J}^{\text{T}} \in \mathbb{R}^{3\times 2}$ yielded:

$$\mathbf{J}^{\text{T}} = -\begin{pmatrix} \mathbf{m}_1 \times \mathbf{u}_1 & \mathbf{m}_2 \times \mathbf{u}_2 \end{pmatrix} \tag{25}$$

 doi:10.20944/preprints202405.1069.v1

In this paper, the friction of the revolute joint was not considered. Then the component of the torque $\boldsymbol{\tau}_{\text{in}}$ in the X-axis direction, denoted as $\tau_{\text{in-x}} \in \mathbb{R}$, yielded

$$\tau_{\text{in-x}} = 0 \tag{26}$$

In the OYZ plane of the coordinate system {S}, (24) could be written as

$$\tau_{\text{ex-x}} - \frac{m_1 s_1 \sin(\varphi_{1,0} + \theta_{\text{x}})}{c_1} t_1 + \frac{m_2 s_2 \sin(\varphi_{2,0} - \theta_{\text{x}})}{c_2} t_2 = 0 \tag{27}$$

where $\tau_{\text{ex-x}} \in \mathbb{R}$ represented the component of the torque $\boldsymbol{\tau}_{\text{ex}}$ in the X-axis direction. That was

$$\begin{aligned} \tau_{\text{ex-x}} &= \frac{m_1 s_1 \sin(\varphi_{1,0} - \theta_{\text{x}})}{c_1} t_1 - \frac{m_2 s_2 \sin(\varphi_{2,0} - \theta_{\text{x}})}{c_2} t_2 \\ &= \begin{pmatrix} \dfrac{m_1 s_1 \sin(\varphi_{1,0} + \theta_{\text{x}})}{c_1} & -\dfrac{m_2 s_2 \sin(\varphi_{2,0} - \theta_{\text{x}})}{c_2} \end{pmatrix} \begin{pmatrix} t_1 \\ t_2 \end{pmatrix} \\ &= \mathbf{J}_{\text{x}}^{\text{T}} \, \mathbf{T} \end{aligned} \tag{28}$$

where $\mathbf{J}_{\text{x}}$ was given in (12).

When the component of torque acted on the movable platform of 1-DOF joint module increased from $\tau_{\text{ex-x}}$ to $\tau_{\text{ex-x}} + \mathrm{d}\tau_{\text{ex-x}}$, the movable platform would rotate slightly around the X axis of {S}, and the increment of the angular displacement would be denoted as $\mathrm{d}\theta_{\text{x}}$. The torque increment $\mathrm{d}\tau_{\text{ex-x}}$ and the angular increment $\mathrm{d}\theta_{\text{x}}$ yielded:

$$\mathrm{d}\tau_{\text{ex-x}} = K_{\theta_{\text{x}}} \mathrm{d}\theta_{\text{x}} \tag{29}$$

where $K_{\theta_{\text{x}}} \in \mathbb{R}$ represented the stiffness of the 1-DOF joint module around the X axis of {S}.

Differentiating on both sides of (28), it yielded:

$$\mathrm{d}\tau_{\text{ex-x}} = \mathrm{d}\mathbf{J}_{\text{x}}^{\text{T}} \, \mathbf{T} + \mathbf{J}_{\text{x}}^{\text{T}} \, \mathrm{d}\mathbf{T} \tag{30}$$

Writing $\mathrm{d}\mathbf{J}_{\text{x}}^{\text{T}} \, \mathbf{T}$ as:

$$\mathrm{d}\mathbf{J}_{\text{x}}^{\text{T}} \, \mathbf{T} = D_{\text{x}} \, \mathrm{d}\theta_{\text{x}} \tag{31}$$

where $D_{\text{x}} \in \mathbb{R}$ was defined as:

$$D_{\text{x}} = \frac{\mathrm{d}\mathbf{J}_{\text{x}}^{\text{T}}}{\mathrm{d}\theta_{\text{x}}} \mathbf{T} \tag{32}$$

Substituting (12) into (32), it yielded:

$$\begin{aligned} D_{\text{x}} = & \frac{m_1 s_1 c_1^2 \cos(\varphi_{1,0} + \theta_{\text{x}}) - m_1^2 s_1^2 \sin^2(\varphi_{1,0} + \theta_{\text{x}})}{c_1^3} t_1 \\ & - \frac{m_2 s_2 c_2^2 \cos(\varphi_{2,0} - \theta_{\text{x}}) + m_2^2 s_2^2 \sin^2(\varphi_{2,0} - \theta_{\text{x}})}{c_2^3} t_2 \end{aligned} \tag{33}$$

In addition, according to (11), we had:

$$\mathrm{d}\mathbf{l}_{\text{c}} = \mathbf{J}_{\text{x}} \, \mathrm{d}\theta_{\text{x}} \tag{34}$$

 doi:10.20944/preprints202405.1069.v1

Then $\mathrm{d}\mathbf{T}$ could be written as:

$$\mathrm{d}\mathbf{T} = \mathbf{K}_{\text{diag}}\mathrm{d}\mathbf{l}_{\text{c}} = \mathbf{K}_{\text{diag}}\ \mathbf{J}_{\text{x}}\ \mathrm{d}\theta_{\text{x}} \tag{35}$$

where $\mathbf{K}_{\text{diag}} = \begin{pmatrix} k_1 & 0 \\ 0 & k_2 \end{pmatrix} \in \mathbb{R}^{2\times 2}$. Here, k_i represented the stiffness of the i^{th} $(i=1,2)$ wire with the VSU in series. Since the stiffness of the wire was far greater than the stiffness of the VSU, then $k_i \approx k_{\text{v}i}$ $(i=1,2)$, where $k_{\text{v}i} \in \mathbb{R}$ was the stiffness of the VSU placed in the i^{th} $(i=1,2)$ wire.

Substituting (31) and (35) into (30), it yielded:

$$\mathrm{d}\tau_{\text{ex-x}} = D_{\text{x}}\ \mathrm{d}\theta_{\text{x}} + \mathbf{J}_{\text{x}}^{\text{T}}\ \mathbf{K}_{\text{diag}}\ \mathbf{J}_{\text{x}}\ \mathrm{d}\theta_{\text{x}} = \left(D_{\text{x}} + \mathbf{J}_{\text{x}}^{\text{T}}\ \mathbf{K}_{\text{diag}}\ \mathbf{J}_{\text{x}}\right)\mathrm{d}\theta_{\text{x}} \tag{36}$$

Then the stiffness of the 1-DOF joint module around the X axis of {S}, $K_{\theta_{\text{x}}} \in \mathbb{R}$, could be written as

$$K_{\theta_{\text{x}}} = D_{\text{x}} + \mathbf{J}_{\text{x}}^{\text{T}}\ \mathbf{K}_{\text{diag}}\ \mathbf{J}_{\text{x}} \tag{37}$$

For a certain pose of the 1-DOF joint module, the matrix $\mathbf{J}_{\text{x}}$ was constant. According to (28), when the component of the external torque, $\tau_{\text{ex-x}}$, was given and one of the wire tension was determined, another wire tension could be calculated. According to (37), the stiffness of the 1-DOF joint module could be adjusted by controlling the wire tensions.

5. Wire Tension Analysis of the Symmetric Joint Module

Since the wire could only pull, but not push, the wire-actuated joint module was actuated redundantly. According to the kinematics and stiffness analysis of the 1-DOF joint module, the wires of the 1-DOF joint module could be divided into two groups. Each group included one wire. The pose of the 1-DOF joint module could be adjusted by controlling the length of one wire, and the stiffness of the 1-DOF joint module could be adjusted by controlling the tension of another wire. It meant that the pose and stiffness of the 1-DOF joint module could be controlled synchronously. For a desired pose of the 1-DOF joint module, $\theta_{\text{x-des}} \in \mathbb{R}$, the corresponding wire lengths could be solved from (7) and (8) easily. For a desired stiffness of the 1-DOF joint module, $K_{\theta_{\text{x}}\text{-des}} \in \mathbb{R}$, the issue of finding out the corresponding wire tensions was called stiffness-oriented wire tension distribution (SWTD) problem.

According to the stiffness model (37) of the 1-DOF joint module, the desired stiffness $K_{\theta_{\text{x}}\text{-des}}$ yielded:

$$K_{\theta_{\text{x}}\text{-des}} = D_{\text{x}} + \mathbf{J}_{\text{x}}^{\text{T}}\mathbf{K}_{\text{diag}}\mathbf{J}_{\text{x}} \tag{38}$$

According to the equilibrium equation (28) of the 1-DOF joint module, when the pose and external force were given, $\tau_{\text{ex-x}}$ and $\mathbf{J}_{\text{x}}$ were both constant. The wire tension t_1 could be expressed by a function of the wire tension t_2, i.e.,

$$t_1 = \frac{m_2 s_2 c_1 \sin(\varphi_{2,0} - \theta_{\text{x}})}{m_1 s_1 c_2 \sin(\varphi_{1,0} + \theta_{\text{x}})} t_2 + \frac{c_1 \tau_{\text{ex-x}}}{m_1 s_1 \sin(\varphi_{1,0} + \theta_{\text{x}})} \tag{39}$$

Substituting (39) into (38), we had a quadratic equation with one variable t_2. Solving t_2 from the quadratic equation and substituting t_2 into (39), the wire tension t_1 could be obtained. Then the two wire tensions t_1 and t_2 were both found out for the desired stiffness $K_{\theta_{\text{x}}\text{-des}}$. That meant the SWTD problem of the 1-DOF joint module was solved.

 doi:10.20944/preprints202405.1069.v1

In order to avoid the actuation wire be slack, a lower limit of the wire tension $t_{\min} \in \mathbb{R}$ was set. In order to avoid the tension of the actuation wire exceeding the capacity of the wire driving unit and the VSU, an upper limit of the wire tension $t_{\max} \in \mathbb{R}$ was set. In this paper, we set $t_{\min} = 100$ N, $t_{\max} = 900$ N. The solved wire tensions in the safe interval $(t_{\min}, t_{\max})$ were called the feasible wire tensions.

6. Simulation Verification

To verify the proposed analysis and method, a simulation example was carried out. The 1-DOF joint module for simulation was shown in Figure 6, and its dimension parameters were given below:

(a) the distance between the wire hole S_i $(i=1,2)$ and the center O_S of the static platform:

$$\overline{\mathrm{O_S S_1}} = \overline{\mathrm{O_S S_2}} = 0.070 \text{ m}$$

(b) the distance between the wire hole M_i $(i=1,2)$ and the center O_M of the movable platform:

$$\overline{\mathrm{O_M M_1}} = \overline{\mathrm{O_M M_2}} = 0.050 \text{ m}$$

(c) the distance between the center O_S of the static platform and the center O of the revolute joint:

$$h_\mathrm{S} = \overline{\mathrm{OO_S}} = 0.080 \text{ m}$$

(d) the distance between the center O_M of the movable platform and the center O of the revolute joint:

$$h_\mathrm{M} = \overline{\mathrm{OO_M}} = 0.060 \text{ m}$$

Based on the dimension parameters of the 1-DOF joint module given above, the parameters $m_i = \overline{\mathrm{OM}_i}$, $s_i = \overline{\mathrm{OS}_i}$, $\varphi_{i,0}$ $(i=1,2)$ could be calculated:

$$m_i = \overline{\mathrm{OM}_i} = \sqrt{\overline{\mathrm{O_M M}_i}^2 + \overline{\mathrm{OO_M}}^2} \approx 0.0781 \text{ m} \tag{40}$$

$$s_i = \overline{\mathrm{OS}_i} = \sqrt{\overline{\mathrm{O_S S}_i}^2 + \overline{\mathrm{OO_S}}^2} \approx 0.1063 \text{ m} \tag{41}$$

$$\varphi_{i,0} = \pi - \angle \mathrm{M}_i\mathrm{OO_M} - \angle \mathrm{S}_i\mathrm{OO_S} \approx 1.7280 \text{ rad} \tag{42}$$

When the pose of the 1-DOF joint module, θ_x, was given, the parameters $\varphi_i = \angle \mathrm{M}_i\mathrm{OS}_i$, $c_i = \overline{\mathrm{M}_i\mathrm{S}_i}$ $(i=1,2)$ could also be calculated according to (4), (5), (7) and (8), respectively.

In order to verify the solution to the SWTD problem of the 1-DOF joint module, two simulation cases were set for different poses and external loads of the 1-DOF joint module, named Case 1 and Case 2 respectively. For Case i $(i=1,2)$, two sub-cases were set for different desired stiffness, named Case i-a and Case i-b $(i=1,2)$ respectively. The cases of the simulation were listed in Table 1.

Table 1. Simulation cases for the SWTD problem of the 1-DOF joint module.

Case	External loads $\tau_{\text{ex-x}}$ (Nm)	Pose θ_x (rad)	Desired stiffness $K_{\theta_\mathrm{x}\text{-des}}$ (Nm/rad)	Wire tension $\mathbf{T} = (t_1 \quad t_2)^\mathrm{T}$ (N)
Case 1-a	2	0.0524	368.66	$(194.77 \quad 150.58)^\mathrm{T}$
Case 1-b	2	0.0524	315.14	$(162.93 \quad 120)^\mathrm{T}$
Case 2-a	-2	0.0349	324.25	$(131.28 \quad 160)^\mathrm{T}$
Case 2-b	-2	0.0349	291.54	$(110.47 \quad 140)^\mathrm{T}$

 doi:10.20944/preprints202405.1069.v1

Here, we took Case 1-a as an example to illustrate the solution to the SWTD problem of the 1-DOF joint module. For the given pose $\theta_x = 0.0524$ rad, the parameters D_x and $\mathbf{J}_x$ could be calculated according to (33) and (12), respectively

$$D_x = -8.12 \tag{43}$$

$$\mathbf{J}_x = \begin{pmatrix} 0.0562 & -0.0597 \end{pmatrix}^{\mathrm{T}} \tag{44}$$

Substituting $\tau_{\text{ex-x}} = 2$ Nm and $\theta_x = 0.0524$ rad into (39), the wire tension t_1 could be obtained by the expression wire tension t_2:

$$t_1 = 1.0614 t_2 + 35.5662 \tag{45}$$

Substituting the desired stiffness $K_{\theta_x\text{-des}} = 282.81$ Nm/rad and (45) into (38), a quadratic equation of t_2 was obtained:

$$0.0033 t_2^2 + 0.88 t_2 - 207.3333 = 0 \tag{46}$$

Solving (46), we had the wire tension $t_2 = 150.58$ N. Substituting t_2 into (45), we obtained the wire tension $t_1 = 194.77$ N. The wire tension t_1 and t_2 were both in the safe interval $(t_{\min}, t_{\max})$. In summary, for Case 1-a, the feasible wire tensions for the desired stiffness were $t_1 = 194.77$ N and $t_2 = 150.58$ N.

Similar to Case 1-a, the wire tension solutions to the SWTD problem of the 1-DOF joint module for the other simulation cases could be obtained. The results of the simulation were listed in Table 1.

7. Conclusion

In this paper, a modular wire-actuated robotic arm was proposed to improve the safety and adaptability of service robots during human-robot interaction, which consisted of three symmetric joint modules in series. To raise the stiffness adjustment range of the robotic arm, a variable-stiffness unit (VSU) was designed based on flexure, which had simple, symmetric and compact structure. The FEA result shown that the VSU yielded lowly nonlinear stiffness-force relationship. In this paper, we focused on the research of the 1-DOF joint module, including kinematics, statics, stiffness and wire tension analysis. It shown that the pose of the joint module could be adjusted by controlling the length of the wires, and the stiffness of the joint module could be adjusted by controlling the tension of the wires. Due to the actuation redundancy, the wires could be divided into two groups, and the pose and stiffness of the joint module could be controlled synchronously. For a given desired stiffness, in order to find out the corresponding wire tensions, the stiffness-oriented wire tension distribution (SWTD) problem should be solved. In this paper, a directly method was proposed for the SWTD problem of the 1-DOF joint module. A simulation was carried out to verify the effectiveness of the proposed analysis and method.

Author Contributions: Conceptualization, K.Y.; formal analysis, K.Y., C.Q., Y.R., and J.H.; methodology, K.Y., C.Q., Y.R., and J.H.; validation, Z.S.; writing-original draft, C.Q.; writing-review and editing, C.W. and C.X.; supervision, K.Y. All authors have read and agreed to the published version of the manuscript.

Funding: This research was funded by Public Welfare Technology Research Program of Zhejiang Province, China (Grant number: LGF22E050003), Public Welfare Technology Research Program of Ningbo City, China (Grant number: 2022S130), Key Research and Development Program of Ningbo City, China (Grant number: 2022Z062).

Data Availability Statement: Data are contained with the article.

Conflicts of Interest: The authors declare no conflicts of interest.

 doi:10.20944/preprints202405.1069.v1

References

1. Tang, Y.; Zhang, Q.; Lin, G.; Yin, J.; Switchable adhesion actuator for amphibious climbing soft robot. *Soft Robot.* **2018**, 5(5): 592-600. https://doi.org/10.1089/soro.2017.0133.
2. Tian, B.; Gao, H.; Yu, H.; Shan, H.; Hou, J.; Yu, H.; Deng, Z. Cable-driven legged landing gear for unmanned helicopter: Prototype design, optimization and performance assessment. *Sci. China Technol. Sc.* **2024**, 67: 1196-1214. https://doi.org/10.1007/s11431-023-2585-8.
3. Yoon, J.; Lee, D.; Bang, J.; Shin, H.G.; Chung, W.K.; Choi, S.; Kim, K. Cable-driven haptic interface with movable bases achieving maximum workspace and isotropic force exertion. *IEEE T. Haptics* **2023**, 16(3): 365-378. https://doi.org/10.1109/TOH.2023.3286353.
4. Mailhot, N.; Abouheaf, M.; M.; Spinello, D. Model-free force control of cable-driven parallel manipulators for weight-shift aircraft actuation. *IEEE T. Instrum. Meas.* **2024**, 73: 2505108. https://doi.org/10.1109/TIM.2023.3346524
5. Axinte, D.; Dong, X.; Palmer, D.; Rushworth, A.; Guzman, S.C.; Olarra, A.; Arizaga, I.; Gomez-Acedo, E.; Txoperena, K.; Pfeiffer, K.; Messmer, F.; Gruhler, M.; Kell, J. MiRoR-miniaturised robotic systems for holistic in-situ repair and maintenance works in restrained and hazardous environments. *IEEE-ASME T. Mech.* **2018**, 23(2): 978-981. https://doi.org/ 10.1109/TMECH.2018.2800285
6. Troncoso, D.A.; Robles-Linares, J.A.; Russo, M.; Elbanna, M.A.; Wild, S.; Xin Dong, Mohammad, A.; Kell, J.; Norton, A.D.; Axinte, D. A continuum robot for remote applications: From industrial to medical surgery with slender continuum robots. *IEEE Robot. Autom. Mag.* **2023**, 30(3): 94-105. https://doi.org/10.1109/MRA.2022.3223220
7. Dong, X.; Wang, M.; Mohammad, A.; Ba, W.; Russo, M.; Norton, A.; Kell, J.; Axinte, D. Continuum robots collaborate for safe manipulation of high-temperature flame to enable repairs in challenging environments. *IEEE-ASME T. Mech.* 2022, 27(5): 4217-4220. https://doi.org/10.1109/TMECH.2021.3138222
8. Choi H, C.; Kang, B.B.; Jung, B.; Cho, K.J. Exo-wrist: a soft tendon-driven wrist-wearable robot with active anchor for dart-throwing motion in hemiplegic patients. *IEEE Robot. Autom. Let.* **2019**, 4(4): 4499-4506. https://doi.org/10.1109/LRA.2019.2931607
9. Pu, S.W.; Pei Y.C.; Chang J.Y. Decoupling finger joint motion in an exoskeletal hand: a design for robot-assisted rehabilitation. *IEEE T. Ind. Electron.* **2020**, 67(1): 686-697. https://doi.org/10.1109/TIE.2019.2912793
10. Wang, X.; Guo, S.; Bai, S. A cable-driven parallel hip exoskeleton for high-performance walking assistance. *IEEE-ASME T. Mech.* **2024**, 71(3): 2705-2715. https://doi.org/ 10.1109/TIE.2023.3270494
11. Xu, M.; Zhou, Z.; Wang, Z.; Zezheng Wang, Ruan, L.; JMai, J.; Wang, Q. Bioinspired cable-driven actuation system for wearable robotic devices: Design, control, and characterization. *IEEE T. Robot.* **2024**, 40: 520-539. https://doi.org/10.1109/TRO.2023.3324200
12. Liao, H.; Chan, H.H.; Liu, G.; Zhao, X.; Gao, F.; Tomizuka, M.; Liao, W.H. Design, control, and validation of a novel cable-driven series elastic actuation system for a flexible and portable back-support exoskeleton. *IEEE T. Robot.* **2024**, 40: 2769-2790. https://doi.org/ 10.1109/TRO.2024.3381556
13. Nakka, S.; Vashista, V. External dynamics dependent human gait adaptation using a cable-driven exoskeleton. *IEEE Robot. Autom. Let.* **2023**, 8(9): 6036-6043. https://doi.org/ 10.1109/LRA.2023.3302189
14. Wu, Z.; Li, Q.; Zhao, J.; Gao, J.; Xu, K. Design of a modular continuum-articulated laparoscopic robotic tool with decoupled kinematics. *IEEE Robot. Autom. Let.* **2019**, 4(4): 3545-3552. https://doi.org/10.1109/LRA.2019.2927929
15. Rivas-Blanco, I.; Lopez-Casado, C.; Perez-Del-Pulgar, C.J.; García-Vacas, F.; Fraile, J.C.; Muñoz, V.F. Smart cable-driven camera robotic assistant. *IEEE T. Hum-Mach Syst.* **2018**, 48(2): 183-196. https://doi.org/10.1109/THMS.2017.2767286
16. Wang, W.; Wang, J.; Chen, C.; Luo, Y.; Wang, X.; Yu, L. Design of position estimator for rope driven micromanipulator of surgical robot based on parameter autonomous selection model. *J. Mech. Robot.* **2024**, 16(4): 041005. https://doi.org/10.1115/1.4062464
17. Li, C.; Gu, X.; Ren, H. A cable-driven flexible robotic grasper with Lego-like modular and reconfigurable joints. *IEEE-ASME T. Mech.* **2017**, 22(6): 2757-2767. https://doi.org/10.1109/TMECH.2017.2765081
18. Kim Y.J. Anthropomorphic low-inertia high-stiffness manipulator for high-speed safe interaction. *IEEE T. Robot.* **2017**, 33(6): 1358-1374. https://doi.org/10.1109/TRO.2017.2732354
19. Xiao, H.; Tang, J.; Lyu, S.; Xu, K.; Ding, X. Design and implementation of a synergy-based cable-driven humanoid arm with variable stiffness. *J. Mech. Robot.* **2024**, 16(4): 041002. https://doi.org/10.1109/TRO.2017.2732354
20. Lin, B.; Xu, W.; Li, W.; Yuan, H.; Liang, B. Ex situ sensing method for the end-effector's six-dimensional force and link's contact force of cable-driven redundant manipulators. *IEEE T. Ind. Inform.* **2024**, 20(5): 7995-8006. https://doi.org/0.1109/TII.2024.3369248
21. Li, R.; Liu, Y.; Guo, A.; Shou, M.; Zhao, M.; Zhu, D.; Yang, P.; Lee, C.H. An inchworm-like climbing robot based on cable-driven grippers. *IEEE-ASME T. Mech.* **2024**, 29(2): 1591-1600. https://doi.org/10.1109/TMECH.2023.3307682

22. Xu, W.; Liu, T.; Li, Y. Kinematics, dynamics, and control of a cable-driven hyper-redundant manipulator. *IEEE-ASME T. Mech.* **2018**, 23(4): 1693-1704. https://doi.org/10.1109/TMECH.2018.2842141
23. Wu, L.; Crawford, R.; Roberts, J. Dexterity analysis of three 6-DOF continuum robots combining concentric tube mechanisms and cable-driven mechanisms. *IEEE Robot. Autom. Let.* **2017**, 2(2): 514-521. https://doi.org/10.1109/LRA.2016.2645519
24. Yang, Q.; Zhou, Q.; Zhou, G.; Jiang, M.; Zhao, Z. Inverse kinematics solution method of an adaptive piecewise geometry for cable-driven hyper-redundant manipulator. *J. Mech. Robot.* **2024**, 16(4):041011. https://doi.org/10.1115/1.4062606
25. Dai, Y.; Wang, S.; Wang, X.; Yuan, H. A novel friction measuring method and its application to improve the static modeling accuracy of cable-driven continuum manipulators. *IEEE Robot. Autom. Let.* **2024**, 9(4): 3259-3266. https://doi.org/10.1109/LRA.2024.3363533
26. Yang, H.; Xia, C.; Wang, X.; Xu, W.; Liang, B. An efficient solver for the inverse kinematics of cable-driven manipulators with pure rolling joints using a geometric iterative approach. *Mech. Mach. Theory* **2024**, 196: 105611. https://doi.org/10.1016/j.mechmachtheory.2024.105611
27. Lau. D.; Eden, J.; Oetomo, D.; Halgamuge, K. S. Musculoskeletal static workspace analysis of the human shoulder as a cable-driven robot. *IEEE-ASME T. Mech.* **2015**, 20(2): 978-984. https://doi.org/10.1109/TMECH.2013.2295120
28. Cheng, H.H.; Lau, D. Cable attachment optimization for reconfigurable cable-driven parallel robots based on various workspace conditions. *IEEE T. Robot.* **2023**, 39(5): 3759-3775. https://doi.org/10.1109/TRO.2023.3288838
29. Haghighipanah, M.; Miyasaka, M.; Hannaford, B. Utilizing elasticity of cable-driven surgical robot to estimate cable tension and external force. *IEEE Robot. Autom. Let.* **2017**, 2(3): 1593-1600. https://doi.org/10.1109/LRA.2017.2676347
30. Jamshidifar, H.; Khajepour, A.; Fidan, B.; Rushton, M. Kinematically-constrained redundant cable-driven parallel robots: Modeling, redundancy analysis, and stiffness optimization. *IEEE-ASME T. Mech.* **2017**, 22(2): 921-930. https://doi.org/10.1109/TMECH.2016.2639053
31. Xu, G.; Zhu, H.; Xiong, H.; Lou, Y. Data-driven dynamics modeling and control strategy for a planar n-DOF cable-driven parallel robot driven by n+1 cables allowing collisions. *J. Mech. Robot.* **2024**, 16(5): 051008. https://doi.org/10.1115/1.4062792
32. Mamidi, T.K.; Bandyopadhyay, S. A modular computational framework for the dynamic analyses of cable-driven parallel robots with different types of actuation including the effects of inertia, elasticity and damping of cables. *Robotica* **2024**, 42: 1676-1708. hhttp://dx.doi.org/10.2139/ssrn.4386942
33. Zhang Z.; Cheng, H.H.; Lau, D. Efficient wrench-closure and interference-free conditions verification for cable-driven parallel robot trajectories using a ray-based method. *IEEE Robot. Autom. Let.* **2020,** 5(1): 8-15. https://doi.org/10.1109/LRA.2019.2942203
34. Ding, M.; Zheng, X.; Liu, L.; Guo, J.; Guo, Y. Collision-free path planning for cable-driven continuum robot based on improved artificial potential field. *Robotica* **2024**, 42(5): 1350-1367. https://doi.org/10.1017/S026357472400016X
35. Qin, Y.; Chen, Q.; Ming, C. Adaptive recursive sliding mode based trajectory tracking control for cable-driven continuum robots. *ISA T.* **2024**, 147: 501-510. https://doi.org/10.1016/j.isatra.2024.02.016
36. Han, Z.; Liu, Z.; Meurer, T.; He, W. PDE-based control synthesis for a planar cable-driven continuum arm. *Automatica* **2024**, 163: 1116000. https://doi.org/10.1016/j.automatica.2024.111600
37. Ameri, A.; Molaei, A.; Khosravi, M.A.; Aghdam, A.G.; Javad Dargahi, J.; S. Fazeli, M. A real-time approach to risk-free control of highly redundant cable-driven parallel robots. *IEEE T. Syst. Man Cy-S.* **2024**, 54(5): 2651-2662. https://doi.org/10.1109/TSMC.2023.3349253
38. Cheah, S.K.; Hayes, A.; Caverly, R.J. Adaptive passivity-based pose tracking control of cable-driven parallel robots for multiple attitude parameterizations. *IEEE T. Contr. Syst. T.* **2024**, 32(1): 202-213. https://doi.org/10.1109/TCST.2023.3311099
39. Li, W.; Huang, X.; Yan, L.; Cheng, H.; Liang, B.; Xu, W. Force sensing and compliance control for a cable-driven redundant manipulator. *IEEE-ASME T. Mech.* **2024**, 29(1): 777-788. https://doi.org/10.1109/TMECH.2023.3263922
40. Zhang, B.; Shang, W.; Deng, B.; Shuang Cong, S.; Li, Z. High-precision adaptive control of cable-driven parallel robots with convergence guarantee. *IEEE T. Ind. Electron.* **2024**, 71(7): 7370-7380. https://doi.org/10.1109/TIE.2023.3310012
41. Yang, K.; Chen, C.; Ye, D.; Wu, K.; Zhang, G. Stiffness modelling and distribution of a modular cable-driven human-like robotic arm. *Mech. Mach. Theory* **2023**, 180: 105150. https://doi.org/10.1016/j.mechmachtheory.2022.105150
42. Chen, W.; Fang, X.; Che, J.; Xiong, C. Design and analysis of passive variable stiffness device based on shear stiffening gel. *Smart Mater. Struct.* **2022**, 31: 125007. https://doi.org/10.1088/1361-665X/ac9dd4

 doi:10.20944/preprints202405.1069.v1

43. Zhu, Y.; Wu, Q.; Chen, B.; Xu, D.; Shao, Z. Design and evaluation of a novel torque-controllable variable stiffness actuator with reconfigurability. *IEEE-ASME T. Mech.* **2022**, 27(1): 292-303.https://doi.org/10.1109/TMECH.2021.3063374
44. Zhao, Y.; Chen, K.; Yu, J.; Huang, S. Design of a parallel compliance device with variable stiffness. *P. I. Mech. Eng. C-J Mec.* **2021**, 235(1): 94-107.https://doi.org/10.1177/09544062209325
45. Yang, K.; Yang, G.; Zhang, C.; Chen C.; Zheng, T.; Cui, Y.; Chen, T. Cable tension analysis oriented the enhanced stiffness of a 3-DOF joint module of a modular cable-driven human-like robotic arm, *Appl. Sci-Basel* **2020**, 10(24): 8871-8887. https://doi.org/10.3390/app10248871